The Astrophysical Journal Letters, 927:L11 (9pp), 2022 March 1 https://doi.org/10.3847/2041-8213/ac4fc8

Rotational Modulation of Spectroscopic Zeeman Signatures in Low-mass Stars

Ryan C Terrien[1], Allison Keen[1], Katy Oda[1], Winter Parts(they/them)[2,3], Guðmundur Stefánsson[4,19], Suvrath Mahadevan[2,3], Paul Robertson[5], Joe P. Ninan[2,3,6], Corey Beard[5], Chad F. Bender[7], William D. Cochran[8,9], Katia Cunha[7,10], Scott A. Diddams[11,12], Connor Fredrick[11,12], Samuel Halverson[13], Fred Hearty[2,3], Adam Ickler[1], Shubham Kanodia[2,3], Jessica E. Libby-Roberts[2,3], Jack Lubin[5], Andrew J. Metcalf[11,12,14], Freja Olsen[1], Lawrence W. Ramsey[2,3], Arpita Roy[15,16], Christian Schwab[17], Verne V. Smith[18], and Ben Turner[1]
[1] Carleton College, One North College St., Northfield, MN 55057, USA; rterrien@carleton.edu
[2] Department of Astronomy & Astrophysics, 525 Davey Laboratory, The Pennsylvania State University, University Park, PA 16802, USA
[3] Center for Exoplanets and Habitable Worlds, 525 Davey Laboratory, The Pennsylvania State University, University Park, PA 16802, USA
[4] Department of Astrophysical Sciences, Princeton University, 4 Ivy Lane, Princeton, NJ 08540, USA
[5] Department of Physics & Astronomy, The University of California, Irvine, Irvine, CA 92697, USA
[6] Department of Astronomy and Astrophysics, Tata Institute of Fundamental Research, Homi Bhabha Road, Colaba, Mumbai 400005, India
[7] Steward Observatory, The University of Arizona, 933 N. Cherry Ave, Tucson, AZ 85721, USA
[8] McDonald Observatory and Department of Astronomy, The University of Texas at Austin, 2515 Speedway, Austin, TX 78712, USA
[9] Center for Planetary Systems Habitability, The University of Texas at Austin, 2515 Speedway, Austin, TX 78712, USA
[10] Observatório Nacional/MCTIC, R. Gen. José Cristino, 77, 20921-400 Rio de Janeiro, Brazil
[11] National Institute of Standards & Technology, 325 Broadway, Boulder, CO 80305, USA
[12] Department of Physics, 390 UCB, University of Colorado, Boulder, CO 80309, USA
[13] Jet Propulsion Laboratory, California Institute of Technology, 4800 Oak Grove Drive, Pasadena, CA 91109, USA
[14] Space Vehicles Directorate, Air Force Research Laboratory, 3550 Aberdeen Ave. SE, Kirtland AFB, NM 87117, USA
[15] Space Telescope Science Institute, 3700 San Martin Dr, Baltimore, MD 21218, USA
[16] Department of Physics and Astronomy, Johns Hopkins University, 3400 N Charles St, Baltimore, MD 21218, USA
[17] Department of Physics and Astronomy, Macquarie University, Balaclava Road, North Ryde, NSW 2109, Australia
[18] NSF's NOIRLab, 950 North Cherry Avenue, Tucson, AZ 85719, USA
Received 2021 December 30; revised 2022 January 25; accepted 2022 January 26; published 2022 March 3

Abstract

Accurate tracers of the stellar magnetic field and rotation are cornerstones for the study of M dwarfs and for reliable detection and characterization of their exoplanetary companions. Such measurements are particularly challenging for old, slowly rotating, fully convective M dwarfs. To explore the use of new activity and rotation tracers, we examined multiyear near-infrared (NIR) spectroscopic monitoring of two such stars—GJ 699 (Barnard's Star) and Teegarden's Star—carried out with the Habitable-zone Planet Finder spectrograph. We detected periodic variations in absorption line widths across the stellar spectrum, with higher amplitudes toward longer wavelengths. We also detected similar variations in the strength and width of the 12435.67 Å neutral potassium (K I) line, a known tracer of the photospheric magnetic field. Attributing these variations to rotational modulation, we confirm the known 145 ± 15 day rotation period of GJ 699, and measure the rotation period of Teegarden's Star to be 99.6 ± 1.4 days. Based on simulations of the K I line and the wavelength dependence of the line-width signal, we argue that the observed signals are consistent with varying photospheric magnetic fields and the associated Zeeman effect. These results highlight the value of detailed line profile measurements in the NIR for diagnosing stellar magnetic field variability. Such measurements may be pivotal for disentangling activity and exoplanet-related signals in spectroscopic monitoring of old, low-mass stars.

Unified Astronomy Thesaurus concepts: Stellar rotation (1629); M dwarf stars (982); Stellar activity (1580); Stellar spectral lines (1630); Near infrared astronomy (1093)

1. Introduction

M dwarf stars are common throughout the galaxy (Henry et al. 2006), but there are important open questions about their magnetic activity and exoplanetary systems. Measurements and modeling of magnetic activity on these stars are rapidly improving (Kochukhov 2021), facilitating new insights into their magnetic dynamos, particularly across the transition from partially to fully convective structure (Chabrier & Baraffe 1997). M dwarfs also commonly host exoplanets (Dressing & Charbonneau 2015; Hsu et al. 2020; Sabotta et al. 2021). However, magnetic activity can confuse or mask low-level exoplanetary signals (e.g., Barnes et al. 2014; Lubin et al. 2021), hindering the construction of a census that might reveal the fingerprints of different exoplanet formation or migration mechanisms (e.g., the prevalence of Earth-sized planets around stars of different masses; Burn et al. 2021). Further, the stellar magnetic field plays an important role in star–planet interactions (Zarka 2007; Turnpenney et al. 2018; Vedantham et al. 2020; Mahadevan et al. 2021) and on planetary habitability (e.g., Shields et al. 2016).

The central observables for these areas of inquiry are the stellar rotation period (e.g., Reiners et al. 2014; Newton et al. 2017; Muirhead et al. 2020) and the various manifestations of the stellar magnetic field (Kochukhov 2021). Stellar rotation can modulate the appearance of regions with differing magnetic

[19] Henry Norris Russell Fellow.

fields. As these regions rotate into and out of view, they can drive strong signals in the stellar photometry (Irwin et al. 2011) and spectroscopy (Robertson et al. 2020; Lafarga et al. 2021). Surface magnetic fields can also be observed more directly through the Zeeman effect on magnetically sensitive spectral lines (Kochukhov 2021). This approach has shown promise for M dwarfs, chiefly with the use of spectropolarimetry to target the strong polarization signature of Zeeman splitting (e.g., Morin et al. 2008).

The weaker signals of Zeeman splitting on observed line profiles in the intensity (i.e., Stokes *I*, unpolarized) spectra include line broadening and strengthening (intensification), and depend on the strength of the line, the magnetic sensitivity of the transition, and the Zeeman pattern (Stift & Leone 2003). These effects have been leveraged to estimate the total magnetic fields of several M dwarfs (Moutou et al. 2017; Shulyak et al. 2019) and have also revealed apparent saturation behavior of the dynamo (Reiners et al. 2009; Muirhead et al. 2020). Measurements of unpolarized Zeeman signatures have even revealed rotational modulation in a small number of cases (Kochukhov & Lavail 2017; Klein et al. 2021) and may contribute to the periodic variability observed in numerous lines in M-dwarf spectra (Lafarga et al. 2021).

We describe here a detailed study on the morphology of rotationally modulated changes in the time-series spectra of two fully convective, slowly rotating M dwarfs: GJ 699 (Barnard's Star) and Teegarden's Star. We show that these variations are consistent with manifestations of Zeeman broadening and intensification under a changing magnetic field. These results provide the most detailed evidence yet that long-term monitoring of Zeeman broadening and intensification in the intensity spectra can provide a powerful diagnostic of the magnetic fields of fully convective stars. Further, these results suggest a promising path for reliably identifying activity-induced variations embedded in precise radial velocity (RV) monitoring of exoplanet host targets.

2. Methods

2.1. Observations with the Habitable-zone Planet Finder

We examined the time-series Habitable-zone Planet Finder (HPF) spectra of GJ 699 and Teegarden's Star. HPF (Mahadevan et al. 2012, 2014) is a high-resolution ($R \sim 55{,}000$), stabilized (Stefansson et al. 2016) spectrograph covering 820–1280 nm. Observing from the 10 m Hobby–Eberly Telescope (HET) at the McDonald Observatory in Texas, HPF is optimized for RV surveys of northern mid-to-late M-dwarf stars. HPF is wavelength calibrated using a custom-built laser frequency comb calibration system (Metcalf et al. 2019) and has a stable instrumental response function (Kanodia et al. 2021), enabling an RV precision of $\sim$1 m s^{-1} on-sky (e.g., Lubin et al. 2021).

GJ 699 (M4) and Teegarden's Star (M7) are routinely observed standard stars for HPF, and thus have long and well-sampled baselines. Our sample of the GJ 699 spectra consists of 1095 spectra (corresponding to 126 visits) exceeding a signal-to-noise ratio (S/N) of 100 (at 10700 Å, per reduced spectral pixel) and spanning 2019 April–2021 July. Our sample of Teegarden's Star's spectra contains 155 spectra (82 visits) exceeding the same S/N threshold and spanning 2018 October to 2021 March. These spectra were produced by the standard HPF pipeline `HxRGproc`, which is described further in Ninan et al. (2018), Kaplan et al. (2019), and Metcalf et al. (2019).

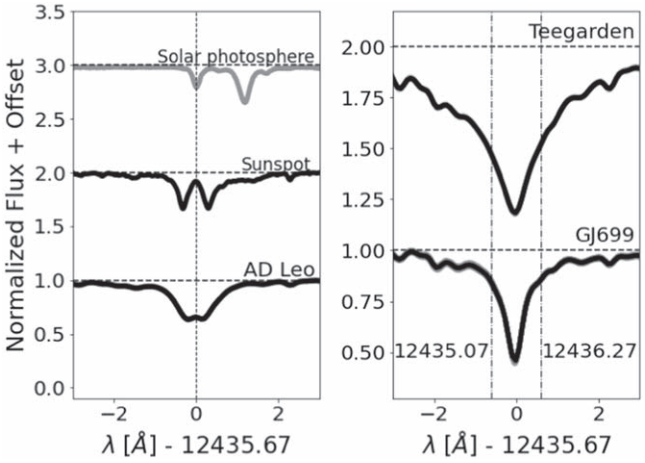

Figure 1. The K I line in multiple stellar spectra, with dashed lines representing the estimated continuum level. The left panel shows comparisons between the solar photosphere (Livingston & Wallace 1991; Wallace et al. 1993) and sunspot spectra (Wallace & Livingston 1992; Wallace et al. 1999), and the highly active M dwarf AD Leonis (with ∼kG magnetic fields), and shows the clear presence of Zeeman splitting for this line. The right panel shows all spectra for each of our target stars overlaid in the vicinity of the K I line, as well as the boundaries used for the equivalent width calculation.

We use a synthetic telluric spectrum (Gullikson et al. 2014) to mask out regions that are affected by telluric contamination.

We evaluated the stability of individual absorption line properties (Section 2.2), as well as average line widths (Section 2.3) in these time-series spectra.

2.2. Line Properties

We examined the well-studied (Fuhrmeister et al. 2022) 12435.67 Å neutral potassium (K I) absorption line, shown in Figure 1. We compiled line properties from the Vienna Atomic Line Database (VALD; Ryabchikova et al. 2015) (air wavelength: 12432.27 Å; transition: $4p\ ^2P^o_{1/2}$–$5s\ ^2S_{1/2}$; effective Landé factor $g_{\rm eff} = 1.3$; $\gamma_{\rm radiative} = 7.74836 \times 10^8$ rad s^{-1}, $\gamma_{\rm Stark} = 1.65657 \times 10^8$ rad s^{-1} per 10^{12} perturbers per cm^3, and $\gamma_{\rm vdW} = 43.57224 \times 10^8$ rad s^{-1} per 10^{16} perturbers per cm^3). This line is exceptionally strong and free of both significant telluric contamination and blending with strong neighboring lines. It exhibits the expected Zeeman splitting in the presence of a magnetic field, as shown in Figure 1 by comparison to solar photospheric (Livingston & Wallace 1991; Wallace et al. 1993) and sunspot (Wallace & Livingston 1992; Wallace et al. 1999) spectra and in HPF spectra of AD Leonis (Figure 1), an M dwarf with well-measured ∼kG magnetic fields (Lavail et al. 2018). This behavior is further confirmed in CARMENES spectra of multiple stars by Fuhrmeister et al. (2022), who also establish that this feature is insensitive to chromospheric variability and therefore a powerful indicator of photospheric properties, including magnetism.

This K I feature appears in the second-reddest HPF spectral order (order index 26, spanning approximately 12367–12525 Å), which is largely clear of telluric contamination. To track the width of the K I line, we measured FWHM_K directly, using the `scipy.signal.peak_widths` function (Virtanen et al. 2020). To track the strength of this line, we measured the (pseudo-)equivalent width (EW_K), defined in the usual way:

$$\mathrm{EW} = \sum_{\lambda_1}^{\lambda_2} (1 - F_\lambda / F_c) d\lambda, \quad (1)$$

where λ_1 and λ_2 are the wavelength limits of the feature (see Figure 1), F_λ is the stellar flux at wavelength λ, and F_c is the continuum flux at λ. We account for fractional pixels at the feature boundaries using a linear interpolation across pixels, and our continuum flux level is defined by the HPF pipeline. In the spectra of GJ 699 and Teegarden's Star, the continuum level is reached at approximately ± 2 Å and ± 5 Å, respectively.

The K I line is notably broader in the spectra of Teegarden's Star than in the warmer GJ 699; this results from the increasing depth of line formation with decreasing temperature, which reveals the increasing effect of collisional broadening with the H_2 molecule (Fuhrmeister et al. 2022, and references therein). Our simulations indicated that the impact of Zeeman intensification would at either temperature be localized to a region near the line core, so we elect to use uniform narrow boundaries for the EW_K calculation. This helps to isolate potential Zeeman-driven variability in the K I line from other nearby spectral variations; tests with broader windows for Teegarden's star were nonetheless consistent with the results presented below.

We estimated the precision of our $FWHM_K$ and EW_K measurements using a Monte Carlo approach and the HPF pipeline-reported variances for each one-dimensional pixel. By measuring each parameter on 100 different realizations of several different HPF spectra of GJ 699 and Teegarden's Star, we estimated the precision of our FWHM measurement at 10 mÅ (∼1%) and 2 mÅ for the equivalent width (EW) measurement (∼0.5%).

2.3. Differential Line Width

To assess the presence of Zeeman broadening, we also examined the average widths of the absorption lines in the stellar spectra using the differential line-width indicator (dLW) as defined and implemented in the SpEctrum Radial Velocity AnaLyzer (SERVAL) pipeline (Zechmeister et al. 2018). To measure the dLWs for HPF spectra, we used the SERVAL pipeline optimized for HPF spectra (Metcalf et al. 2019; Stefansson et al. 2020). Briefly, the SERVAL algorithm involves the construction of a high-S/N template and matching of individual observations against this template. The dLW results from considering the second (spectral) derivative of the template during the matching process and encodes the combined line-width changes across all lines used in the template. The dLW is analogous to the FWHM of the cross correlation function (CCF) but presents a simpler profile in the context of M-dwarf spectra which have many blended lines. In the calculation of the dLW, we mask out spectral regions impacted by tellurics and sky emission lines, as discussed in Stefansson et al. (2020). We estimated the dLW uncertainty as described in Zechmeister et al. (2018) and found a typical per-spectrum precision of 5 m^2 s^{-2} (5%–10%).

To study the dLW behavior as a function of wavelength, we also calculated the dLW for individual spectral orders. Estimating the dLW per order enabled 10 independent measurements (corresponding to HPF's most telluric-free orders) of dLW spanning 840–1250 nm.

2.4. Independent Measurements of Differential Line Width

Teegarden's Star has also been monitored extensively with CARMENES (Zechmeister et al. 2019), which has visible ($R \sim 94{,}600$, 5200–9600 Å) and near-IR (NIR; $R \sim 80{,}400$, 9600–17100 Å) channels. The public data used here consist of 244 measurements in the NIR channel and 245 in the visible channel of the dLW, spanning an observing baseline from 2016 to 2019 and with typical S/N of 58 per extracted pixel around 746 nm.

2.5. Periodicity Measurement

To measure the periodicity of modulations present in our spectroscopic indicators, we employed the generalized Lomb–Scargle (GLS) periodogram (Zechmeister & Kürster 2009), as implemented in `astropy` (Astropy Collaboration et al. 2013, 2018). We searched frequencies corresponding to periods of 3–500 days, using a frequency grid sufficiently dense to provide 10 samples across a given periodogram peak. We estimated the false-alarm probability using the method described in Baluev (2008), following similar recent work (Lafarga et al. 2021).[20]

2.6. Simulations

To assess whether the observed variations were consistent with variable Zeeman splitting, we simulated the K I line using the `NICOLE` (Socas-Navarro et al. 2015) program, with plane-parallel Model Atmospheres in Radiative and Convective Scheme (MARCS) atmosphere (Gustafsson et al. 2008) inputs corresponding approximately to GJ 699 and Teegarden's Star (3300 K, [Fe/H] = 0.0 and 2900 K, [Fe/H] = −0.25, respectively, and $\log(g) = 5.0$, no microturbulence) and line parameters extracted from the Vienna Atomic Line Database (VALD; given above).

For each star, we manually adjusted the K abundance to approximately match the depth of the observed line profile. For Teegarden's Star, we used [K] = 4.92[21], and for GJ 699, we used [K] = 4.62. These values are generally consistent with the old age and subsolar metallicity estimates for both stars (Muirhead et al. 2012; Zechmeister et al. 2019), though we emphasize that our goal in this work is not precise abundance determination but to look at the temporal variability of the line. We set the macroturbulent velocity to 1 km s^{-1} for both stars, in order to approximately match the observed line widths. For simplicity, we assumed local thermodynamic equilibrium (LTE) in these simulations. We caution that departures from LTE are expected for other K I lines in cool stars (e.g., Reggiani et al. 2019) and may impact the comparison between simulated and observed spectra, although Reggiani et al. (2019) found minimal departures from LTE for the low temperatures and high log(g) values associated with M dwarfs.

We implemented a radially oriented two-component magnetic field strength distribution, described by a magnetic field strength B and a filling fraction f (Kochukhov 2021), which are uniform for all simulated lines of sight.

We disk-integrated over the visible hemisphere of the star by first simulating in `NICOLE` a series of 512 one-dimensional spectra along a line from disk center to disk edge. These spectra were evenly spaced in a projected radius from the disk center, and account for the effect of limb darkening as well as the changing angle between the magnetic field and the line of sight. To account for stellar rotational broadening, we applied

[20] We note that the interpretation of periodogram peak significance is not necessarily straightforward, and we refer the reader to VanderPlas (2018) and references therein for a discussion of the related caveats and implications.

[21] Abundances quoted on the usual logarithmic scale as $\log(N_K/N_H) + 12.0$.

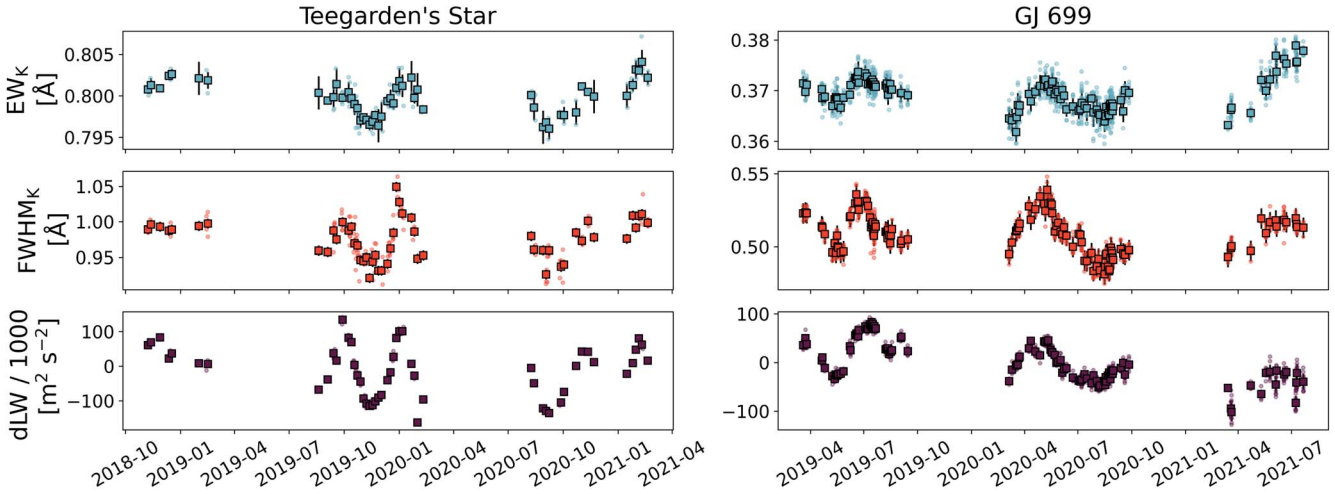

Figure 2. EW$_K$ (top), FWHM$_K$ (middle), and dLW (bottom) as measured for Teegarden's Star (left) and GJ 699 (right) with HPF. Individual measurements are shown as points, while boxes show binned averages (daily for GJ 699, 5 days for the more sparsely sampled Teegarden's Star) with error bars corresponding to either (1) the measured scatter within that day if multiple spectra are obtained, or (2) the baseline single-measurement precision estimate if only one spectrum was taken during the relevant bin. Significant periodic variations are present in all measurements and are largely in-phase across these separate measurements.

appropriate Doppler shifts to each line of sight assuming rigid-body rotation perpendicular to the line-of-sight and rotational periods corresponding to the measured period for each star (see Section 3.2). We then formed the disk-integrated line profile by integrating over the rotating and limb-darkened lines of sight.

3. Results

We detected significant periodic variations in the K I widths and strengths (FWHM$_K$, EW$_K$) and in the general line widths (dLWs), consistent with rotational modulation of Zeeman intensification and Zeeman broadening. We detail these results, and their interpretation, below.

3.1. Spectroscopic Measurements

The time-series measurements of FWHM$_K$, EW$_K$, and dLW in GJ 699 and Teegarden's Star are shown in Figure 2 and reveal significant, similar, long-term variations over >2 yr. FWHM$_K$ varies at the 50–100 mÅ level (∼10%), EW$_K$ varies at the 5–10 mÅ level (0.5%–3%), while the dLWs vary at $\gtrsim$100 m^2 s^{-2}. The amplitudes of these variations exceed the estimated per-spectrum uncertainties.

Figure 3 shows the dLW measurements in detail. CARMENES data dramatically extend the dLW baseline for Teegarden's Star. CARMENES data from both the visible and NIR channels show a long-term periodicity, which is consistent with the variations detected with HPF. This is discussed in more detail in Section 4.

We also examined the dLW measurements at different wavelengths by comparing the HPF and CARMENES dLW values (for Teegarden's Star), as well as the per-order dLW measured in the HPF spectra (Figure 3). A trend of increasing variability amplitude with increasing wavelength is apparent for both stars in the per-order dLW values and between instruments for Teegarden's Star. As discussed below, this increasing amplitude with wavelength is expected of Zeeman broadening (Reiners 2012).

To gain insight into the behavior of the K I line, we also examined the line-shape change between epochs of low and high EW$_K$, as shown in Figure 4. This figure confirms that higher EW$_K$ correlates with a broader line profile (as suggested in Figure 2) and also with a shallower line core.

We also explored whether the variation observed in EW$_K$ and FWHM$_K$ is consistent with what might be produced by rotational modulation of magnetic features on the surfaces of GJ 699 and Teegarden's Star, using the simulations described in Section 2.6. Figure 4 shows the resulting variation of the line-shape parameters when the magnetic field strength and filling factor of our two-component model are varied. We note that the EW$_K$ and FWHM$_K$ are dependent on the precise choice of continuum level, which cannot be defined equivalently in the observed and simulated spectra, because the latter has only a single source of opacity. We therefore include an offset for each of these quantities to align the simulated and measured values, and we emphasize that the relevant comparison here is the range of variation.

For both stars, we observe that the range of variation and the measured line shapes themselves can be approximately reproduced by magnetic field strength and filling factor variations in the simulated spectra (Figure 4). We note that our two-component model is likely a significant oversimplification of the true magnetic field configuration, and that there are numerous degeneracies between the line profile measurements and the line parameters adopted for these simulations which complicate the reliable determination of a single magnetic field and filling factor for a given spectrum.[22] Nonetheless, we conclude that the range of variations observed in our line profile measurements can at least be plausibly explained by variations in our magnetic field model.

3.2. Rotation Period Measurements

The GLS periodogram results for our measurements, including the periods of the most significant peaks, are shown in Figure 5. For GJ 699, the most recent observing season appears qualitatively different from the previous two; this change may be related to a recently uncovered detector bias

[22] One complication is between the absorbing species abundance and magnetic field strength; properly disentangling these two properties can be accomplished, for example, if another absorption line from the same species is accessible and has $g_{\rm eff} = 0$. (e.g., Shulyak et al. 2019).

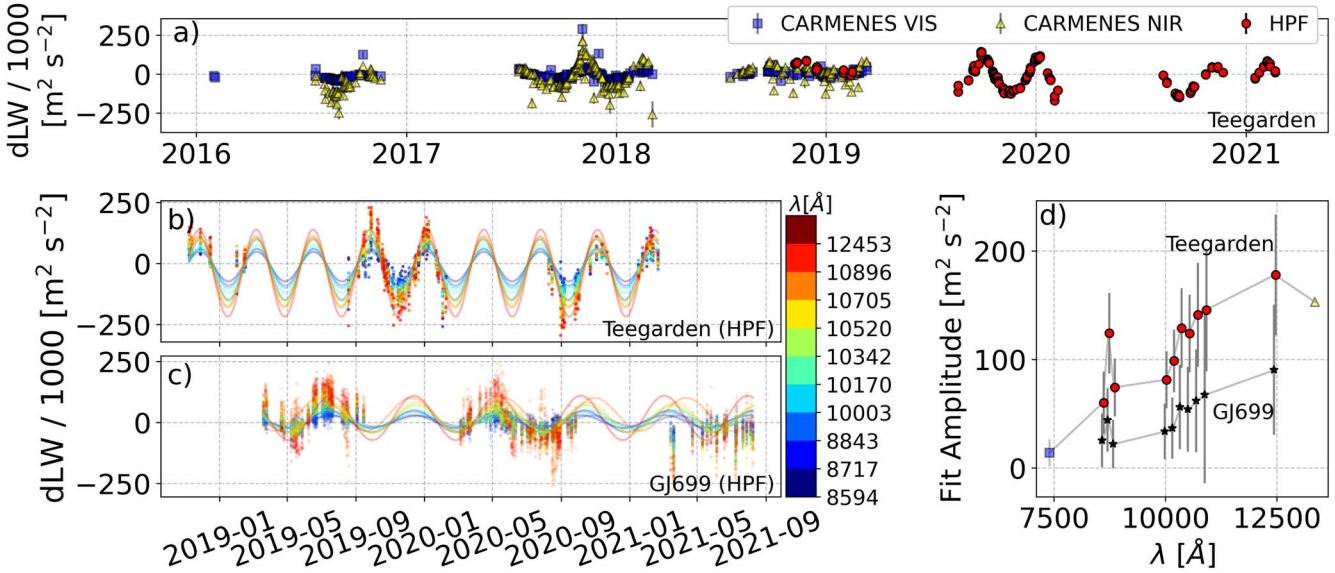

Figure 3. (a) Time-series dLW measurements for Teegarden's Star from HPF and CARMENES visible (VIS) and infrared (NIR) channels (Zechmeister et al. 2019). Periodic modulations are detected by both instruments, and are larger in amplitude at infrared wavelengths (HPF, CARMENES-NIR) than at visible wavelengths (CARMENES-VIS). (b) The HPF time-series dLW measurements for Teegarden's Star, separated and color-coded by spectrograph order. Redder (bluer) wavelengths are longer (shorter). Overplotted are the best-fit sinusoids for each wavelength region as determined by the GLS package (Zechmeister & Kürster 2009). (c) The same as (b), but for GJ 699. A consistent oscillatory pattern is clear at each wavelength, and longer wavelengths tend to correspond to higher amplitudes of variation. (d) The amplitudes of the best-fit sinusoids to the order-by-order dLW measurements for Teegarden's Star (circles) and GJ 699 (stars) as a function of wavelength, showing increasing amplitude with wavelength as expected for the Zeeman effect. The black circles for Teegarden's Star are calculated from CARMENES data: the left point (CARMENES-VIS) is taken from a best-fit sinusoid; the amplitude from the noisier CARMENES-NIR data is simply estimated as half of the difference between the 2nd and 98th percentiles. Error bars for all best-fit amplitudes represent the residual rms after the removal of the best-fit sinuosid.

voltage drift. For completeness, we retain these data points in our data set, but for our period analysis we conservatively use only the data through 2020.

For Teegarden's Star, the spectroscopic indicators are unanimous in the detection of a strong periodicity. We estimate the period by taking the mean and standard deviation of the periodogram peaks from the five time series (HPF dLW, Carmenes-NIR and VIS dLW, HPF FWHM$_K$, and HPF EW$_K$), finding 99.6 ± 1.4 days, which we identify with the rotation period.

For GJ 699, we found strong peaks in the periodograms near the suspected 145 ± 15 days rotation period of this star (Toledo-Padrón et al. 2019). Among the HPF time series, the mean and standard deviation of these peak values are 155 days and 2 days, respectively. We note that the time baseline of our data set is smaller than that of Toledo-Padrón et al. (2019), who find a forest of periodogram peaks for GJ 699 at 145 ± 15 days, which may be related to differential rotation. The periodicity detected in our data set is more tightly localized around 155 days; this may be an artifact of the shorter time baseline. Another significant peak in our periodograms around 300 days may be a harmonic of the rotation period or due to a longer-term activity cycle.

4. Discussion

These measurements offer some of the clearest examples yet of rotationally modulated variations in the spectra of slowly rotating, fully convective stars. These measurements enable the recovery of a signal near the rotation period of 145 ± 15 days of GJ 699 (Toledo-Padrón et al. 2019) and allow us to measure the rotation period of Teegarden's Star at 99.6 ± 1.5 days. Notably, dLW modulations at ~100 days are clearly present in the data of Zechmeister et al. (2019), who caution against overinterpreting these variations due to potential contamination from tellurics, instrumental focus changes, and other effects. The consistency of the signal between CARMENES and HPF suggests that it is indeed of stellar origin. Further, this relatively long rotation period is consistent with an old age, indicated by the low Hα emission of Teegarden's Star (Zechmeister et al. 2019).

4.1. Magnetic Origin

We argue that the observed variations are consistent with a changing magnetic field imprinting on the spectra via the Zeeman effect. The indicators (FWHM$_K$, EW$_K$, and dLW) change in phase with each other (Figure 2), and at levels consistent with our simple model of a changing surface magnetic field. Further, the line-width changes are stronger at longer wavelengths (Figure 3), as is expected for Zeeman broadening, in which the wavelength separation of the split line components ($\Delta\lambda$) from the unsplit line center (λ_0) behaves as

$$\Delta\lambda \propto g_{\rm eff} B \lambda_0^2, \quad (2)$$

where $g_{\rm eff}$ is the effective Landé factor and B is the magnetic field (Kochukhov 2021). Finally, the line-shape change of the K I line is consistent with simple simulations of the impact of a changing magnetic field (Figure 4).

We note, however, the potential contribution of other effects on the stellar surface. For example, stellar rotation that brings regions of varying magnetic field strength into and out of view may also modulate the appearance of associated bright/hot regions (faculae) or dark/cool regions (spots). Spot and faculae sizes and filling fractions are not well constrained for these M dwarfs (e.g., Rackham et al. 2018), and we cannot rule out that the combined effects of these regions may be the origin of some of the rotational modulation we observe. However, we do

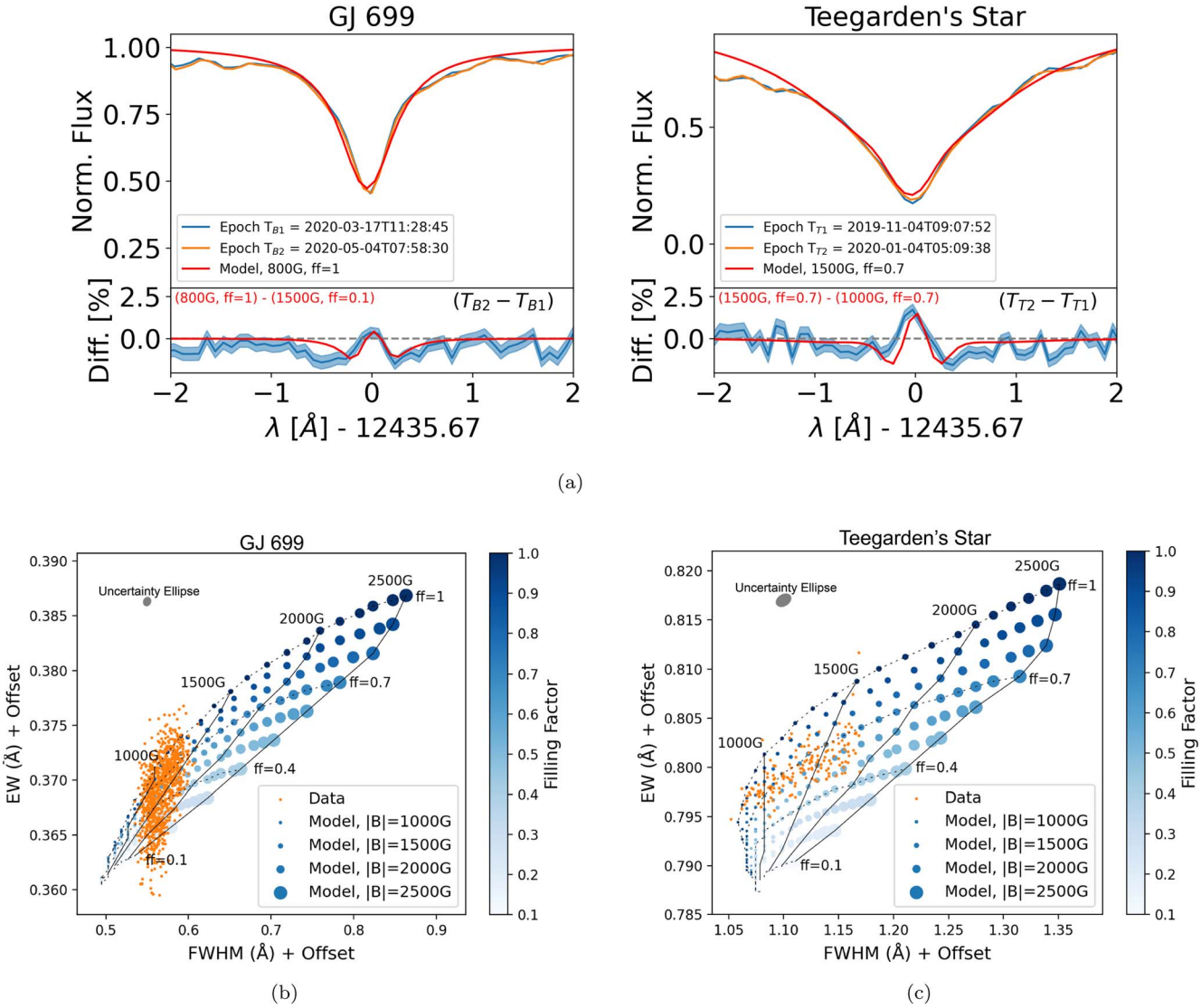

Figure 4. (a) The detailed line profile of the K I line in GJ 699 and Teegarden's Star, showing the change between epochs of low and high EW_K. In each case, epoch 1 (2) corresponds to a period of low (high) EW_K, $FWHM_K$, and dLW. The difference, shown in the bottom panels, reveals a line-shape change (from first to second epochs) that is consistent with a line that is strengthening and broadening under the Zeeman effect (simulated difference overlaid). (b, c) Measured (orange) and simulated (blue) variations over time of K I line EW_K and $FWHM_K$ for (b) GJ 699 and (c) Teegarden's Star. Simulations were generated using `NICOLE` (Socas-Navarro et al. 2015), as described in Section 2.6, varying the magnetic field strength and filling factor. In both stars, the approximate range of variation observed for EW_K and $FWHM_K$ can be reproduced in the simulated spectra. Gray ovals represent the approximate error ellipse, accounting for typical pipeline-reported variances in the measured HPF spectra for each star.

note that in simple (single-temperature) simulations, the K I line becomes both deeper and broader with decreasing temperature, rather than the stronger/shallower behavior shown in Figure 4. This favors the Zeeman explanation over a simple temperature contrast.

A fully self-consistent description of the effect of magnetic fields on the stellar surface would account for the impact of the magnetic fields on the gas dynamics via magnetohydrodynamic simulation. Indeed, the resulting changes of line positions and profile asymmetries are expected to be an important pathway for stellar activity to print through to RV measurements (Meunier et al. 2017), although the dynamics may be somewhat different for M dwarfs than for FGK stars (Liebing et al. 2021). With only the K I line examined in detail, we cannot measure the low-level line asymmetries which accompany changes in the visible convective pattern and so cannot constrain if or how this may impact our measurements. However, we do note that Toledo-Padrón et al. (2019) examined the bisector behavior in GJ 699 and found no detectable signal of changing line asymmetry at their level of measurement precision.

Finally, it is possible that the measured line strengths are also impacted by variable chromospheric emission, which is thought to drive some of the variability in line-by-line studies of correlation with established activity indicators (e.g., Wise et al. 2018). However, Fuhrmeister et al. (2022) considered correlations between the established chromospheric Hα activity indicator and the K I line for a range of M dwarfs and found that it exhibits no measurable chromospheric component (in contrast to K I lines at shorter wavelengths). Further, pure chromospheric "filling-in" of the line core would not be

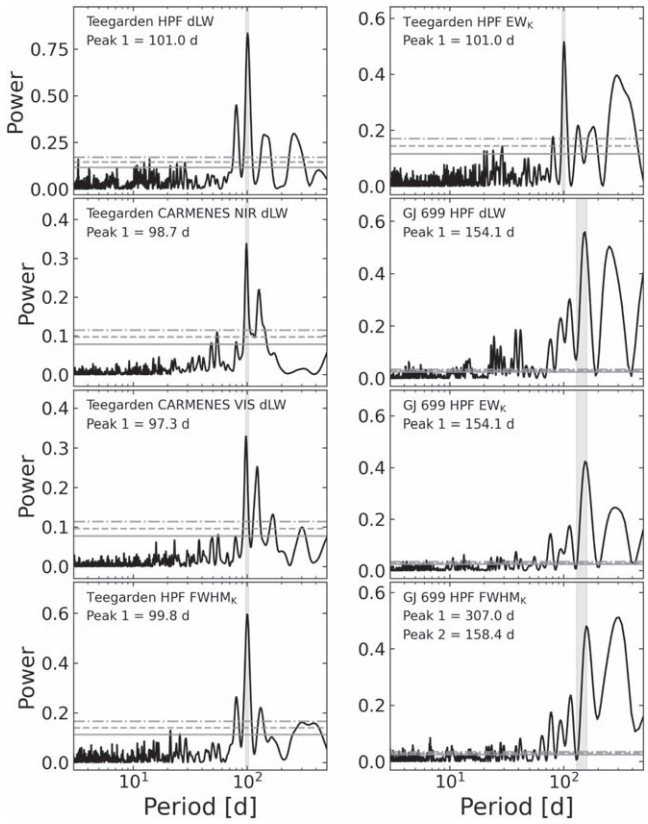

Figure 5. GLS periodograms for Teegarden's Star and GJ 699. In each case, the false-alarm probability estimates for 10% (solid line), 1% (dashed line), and 0.1% (dashed–dotted line) are indicated. For Teegarden's Star, a 99.6 ± 1.5 days periodicity (highlighted) is strong in each of the dLW measurements (HPF, and CARMENES-VIS and -NIR), as well as in the EW_K and $FWHM_K$ measurements. For GJ 699, each indicator has a strong peak at the 145 ± 15 days rotation period (highlighted; Toledo-Padrón et al. 2019).

expected to exhibit the tight correlation observed between EW_K and $FWHM_K$, nor would we expect it to be so widespread across the spectrum as indicated by the dLW measurements.

4.2. Implications

The strength of the rotational modulations stands in contrast to the low photometric variability in both GJ 699 and Teegarden's Star. Careful analysis revealed no rotation period signal in the photometry of Teegarden's Star by Zechmeister et al. (2019), and the rotation period was only marginally detected in some subsets of photometric data used by Toledo-Padrón et al. (2019). The clear spectroscopic detection of rotation in both stars echos the findings of Lafarga et al. (2021), who showed that the rotation period is frequently recoverable in the cross-correlation function parameters, chromospheric indicators, and dLWs of M dwarfs. These findings indicate that spectroscopic monitoring may often provide the best handle on the rotation period for these types of stars.

The need to disentangle stellar activity from exoplanetary signals in RV data is well recognized and has motivated careful statistical (e.g., Davis et al. 2017) and line-by-line (e.g., Dumusque 2018; Wise et al. 2018) analyses to tease these effects apart. To the extent that our observed modulations are driven by the Zeeman effect, this provides a compelling justification for spectroscopic monitoring of RV targets (especially fully convective M dwarfs) at infrared wavelengths, where the Zeeman impact is largest. Together with the results of Lafarga et al. (2021), the K I line studied here appears to provide a powerful indicator of the changing photospheric magnetic field on these stars, which may be expected to perform well as a tracer of rotational modulation and as an RV activity indicator.

Recently, Klein et al. (2021) used Zeeman Doppler imaging to recover the magnetic field geometry of Proxima Centauri, an old, slowly rotating, fully convective star similar to GJ 699 and Teegarden's Star (albeit more active). They additionally found a significant rotational modulation in the Stokes I spectra of Proxima Cen and discuss the value of contrasting polarized and unpolarized indicators for diagnosing the properties of the dynamos of these fully convective stars. Based on the significance of the unpolarized Zeeman signatures presented here, we suggest that long-term spectropolarimetric and spectroscopic monitoring of GJ 699 and Teegarden's Star may prove similarly revealing about the (differential) rotation, dynamo mechanisms, and activity cycles of fully convective stars.

5. Conclusion

We present the detection of significant rotational modulation of absorption line strength and width in the time-series spectra of the slowly rotating, fully convective M dwarfs GJ 699 and Teegarden's Star. By establishing the wavelength dependence of the line-width signal and by comparing to simulations of the expected line-shape change, we argue that these signals are consistent with the expected effect of a changing magnetic field mediated by the Zeeman effect. Using the GLS periodogram technique to measure the periodicities in these signals, we also confirm the rotation period of GJ 699 at 145 ± 15 days, and establish the rotation period of Teegarden's Star at 99.6 ± 1.4 days. The use of these Zeeman tracers in high-resolution stabilized NIR spectra provides a promising approach for the extraction of rotation and magnetic field information for the detailed study of fully convective stars and their exoplanetary companions. The promise of highly stabilized NIR spectrometers is now being realized in their ability to measure and potentially help mitigate even subtle stellar activity signatures.

We thank the anonymous reviewer for prompt feedback that improved the quality of this manuscript.

These results are based on observations obtained with the Habitable-zone Planet Finder Spectrograph on the Hobby–Eberly Telescope (HET). The HET is a joint project of the University of Texas at Austin, the Pennsylvania State University, Ludwig-Maximilians-Universitat Munchen, and Georg-August Universitat Gottingen. The HET is named in honor of its principal benefactors, William P. Hobby and Robert E. Eberly. The HET collaboration acknowledges the support and resources from the Texas Advanced Computing Center. We thank the resident astronomers and telescope operators at the HET for the skillful execution of our observations with HPF.

We acknowledge support from NSF grant Nos. AST 1006676, AST 1126413, AST 1310875, AST 1310885, AST 2009955, AST 2009889, AST 2009982, AST 2009554, and the NASA Astrobiology Institute (NNA09DA76A) in our pursuit of precision radial velocities in the NIR. We also acknowledge support from the Heising-Simons Foundation via grant No. 2017-0494. This research was conducted in part under NSF

grant Nos. AST-2108493, AST-2108512, AST-2108569, and AST-2108801 in support of the HPF Guaranteed Time Observations survey. We also acknowledge support from the NASA Extreme Precision Radial Velocity program via grant No. 80NSSC21K2006. We also acknowledge support from the Carleton College Towsley Endowment, as well as the Minnesota Space Grant Consortium. K.C. and V.S. acknowledge partial support by the National Science Foundation through NSF grant No. AST-2009507.

This work has made use of the VALD database, operated at Uppsala University, the Institute of Astronomy RAS in Moscow, and the University of Vienna.

R.C.T. thanks B. Duffy for his technical assistance with computing resources at Carleton.

We would like to acknowledge that the HET is built on Indigenous land. Moreover, we would like to acknowledge and pay our respects to the Carrizo & Comecrudo, Coahuiltecan, Caddo, Tonkawa, Comanche, Lipan Apache, Alabama-Coushatta, Kickapoo, Tigua Pueblo, and all the American Indian and Indigenous Peoples and communities who have been or have become a part of these lands and territories in Texas, here on Turtle Island.

Facility: 10 m HET (HPF).

Software: `astropy` (Astropy Collaboration et al. 2013, 2018), `numpy` (van der Walt et al. 2011), `scipy` (Virtanen et al. 2020), `HxRGproc` (Ninan et al. 2018), `matplotlib` (Hunter 2007), `GNU Parallel` (Tange 2011), `barycorrpy` (Kanodia & Wright 2018), `SERVAL` (Zechmeister et al. 2018).

ORCID iDs

Ryan C Terrien https://orcid.org/0000-0002-4788-8858
Allison Keen https://orcid.org/0000-0002-9800-9868
Katy Oda https://orcid.org/0000-0001-9770-7624
Winter Parts(they/them) https://orcid.org/0000-0001-7142-2997
Guðmundur Stefánsson https://orcid.org/0000-0001-7409-5688
Suvrath Mahadevan https://orcid.org/0000-0001-9596-7983
Paul Robertson https://orcid.org/0000-0003-0149-9678
Joe P. Ninan https://orcid.org/0000-0001-8720-5612
Corey Beard https://orcid.org/0000-0001-7708-2364
Chad F. Bender https://orcid.org/0000-0003-4384-7220
William D. Cochran https://orcid.org/0000-0001-9662-3496
Katia Cunha https://orcid.org/0000-0001-6476-0576
Scott A. Diddams https://orcid.org/0000-0002-2144-0764
Connor Fredrick https://orcid.org/0000-0002-0560-1433
Samuel Halverson https://orcid.org/0000-0003-1312-9391
Fred Hearty https://orcid.org/0000-0002-1664-3102
Adam Ickler https://orcid.org/0000-0001-5064-9973
Shubham Kanodia https://orcid.org/0000-0001-8401-4300
Jessica E. Libby-Roberts https://orcid.org/0000-0002-2990-7613
Jack Lubin https://orcid.org/0000-0001-8342-7736
Andrew J. Metcalf https://orcid.org/0000-0001-5000-1018
Freja Olsen https://orcid.org/0000-0002-3628-4426
Lawrence W. Ramsey https://orcid.org/0000-0002-4289-7958
Arpita Roy https://orcid.org/0000-0001-8127-5775
Christian Schwab https://orcid.org/0000-0002-0091-7105
Verne V. Smith https://orcid.org/0000-0002-0134-2024
Ben Turner https://orcid.org/0000-0001-5211-9458

References

Astropy Collaboration, Price-Whelan, A. M., Sipőcz, B. M., et al. 2018, AJ, 156, 123
Astropy Collaboration, Robitaille, T. P., Tollerud, E. J., et al. 2013, A&A, 558, A33
Baluev, R. V. 2008, MNRAS, 385, 1279
Barnes, J. R., Jenkins, J. S., Jones, H. R. A., et al. 2014, MNRAS, 439, 3094
Burn, R., Schlecker, M., Mordasini, C., et al. 2021, A&A, 656, A72
Chabrier, G., & Baraffe, I. 1997, A&A, 327, 1039
Davis, A. B., Cisewski, J., Dumusque, X., Fischer, D. A., & Ford, E. B. 2017, ApJ, 846, 59
Dressing, C. D., & Charbonneau, D. 2015, ApJ, 807, 45
Dumusque, X. 2018, A&A, 620, A47
Fuhrmeister, B., Czesla, S., Nagel, E., et al. 2022, A&A, 657, A125
Gullikson, K., Dodson-Robinson, S., & Kraus, A. 2014, AJ, 148, 53
Gustafsson, B., Edvardsson, B., Eriksson, K., et al. 2008, A&A, 486, 951
Henry, T. J., Jao, W.-C., Subasavage, J. P., et al. 2006, AJ, 132, 2360
Hsu, D. C., Ford, E. B., & Terrien, R. 2020, MNRAS, 498, 2249
Hunter, J. D. 2007, CSE, 9, 90
Irwin, J., Berta, Z. K., Burke, C. J., et al. 2011, ApJ, 727, 56
Kanodia, S., & Wright, J. 2018, RNAAS, 2, 4
Kanodia, S., Halverson, S., Ninan, J. P., et al. 2021, ApJ, 912, 15
Kaplan, K. F., Bender, C. F., Terrien, R. C., et al. 2019, in ASP Conf. Ser. 523, Astronomical Data Analysis Software and Systems XXVII, ed. P. J. Teuben et al. (San Francisco, CA: ASP), 567
Klein, B., Donati, J.-F., Hébrard, É. M., et al. 2021, MNRAS, 500, 1844
Kochukhov, O. 2021, A&ARv, 29, 1
Kochukhov, O., & Lavail, A. 2017, ApJL, 835, L4
Lafarga, M., Ribas, I., Reiners, A., et al. 2021, A&A, 652, A28
Lavail, A., Kochukhov, O., & Wade, G. A. 2018, MNRAS, 479, 4836
Liebing, F., Jeffers, S. V., Reiners, A., & Zechmeister, M. 2021, A&A, 654, A168
Livingston, W., & Wallace, L. 1991, An atlas of the solar spectrum in the infrared from 1850 to 9000 cm^{-1} (1.1 to 5.4 micrometer), NSO Technical Report, Tucson, National Solar Observatory, National Optical Astronomy Observatory
Lubin, J., Robertson, P., Stefansson, G., et al. 2021, AJ, 162, 61
Mahadevan, S., Ramsey, L., Bender, C., et al. 2012, Proc. SPIE, 8446, 84461S
Mahadevan, S., Ramsey, L. W., Terrien, R., et al. 2014, Proc. SPIE, 9147, 91471G
Mahadevan, S., Stefánsson, G., Robertson, P., et al. 2021, ApJL, 919, L9
Metcalf, A. J., Anderson, T., Bender, C. F., et al. 2019, Optic, 6, 233
Meunier, N., Lagrange, A. M., Mbemba Kabuiku, L., et al. 2017, A&A, 597, A52
Morin, J., Donati, J. F., Petit, P., et al. 2008, MNRAS, 390, 567
Moutou, C., Hébrard, E. M., Morin, J., et al. 2017, MNRAS, 472, 4563
Muirhead, P. S., Veyette, M. J., Newton, E. R., Theissen, C. A., & Mann, A. W. 2020, AJ, 159, 52
Muirhead, P. S., Johnson, J. A., Apps, K., et al. 2012, ApJ, 747, 144
Newton, E. R., Irwin, J., Charbonneau, D., et al. 2017, ApJ, 834, 85
Ninan, J. P., Bender, C. F., Mahadevan, S., et al. 2018, Proc. SPIE, 10709, 107092U
Rackham, B. V., Apai, D., & Giampapa, M. S. 2018, ApJ, 853, 122
Reggiani, H., Amarsi, A. M., Lind, K., et al. 2019, A&A, 627, A177
Reiners, A. 2012, LRSP, 9, 1
Reiners, A., Basri, G., & Browning, M. 2009, ApJ, 692, 538
Reiners, A., Schüssler, M., & Passegger, V. M. 2014, ApJ, 794, 144
Robertson, P., Stefansson, G., Mahadevan, S., et al. 2020, ApJ, 897, 125
Ryabchikova, T., Piskunov, N., Kurucz, R. L., et al. 2015, PhyS, 90, 054005
Sabotta, S., Schlecker, M., Chaturvedi, P., et al. 2021, A&A, 653, A114
Shields, A. L., Ballard, S., & Johnson, J. A. 2016, PhR, 663, 1
Shulyak, D., Reiners, A., Nagel, E., et al. 2019, A&A, 626, A86
Socas-Navarro, H., de la Cruz Rodríguez, J., Asensio Ramos, A., Trujillo Bueno, J., & Ruiz Cobo, B. 2015, A&A, 577, A7
Stefansson, G., Hearty, F., Robertson, P., et al. 2016, ApJ, 833, 175
Stefansson, G., Cañas, C., Wisniewski, J., et al. 2020, AJ, 159, 100
Stift, M. J., & Leone, F. 2003, A&A, 398, 411
Tange, O. 2011, Gnu parallel-the command-line power tool.; login: The USENIX Magazine, 36, 42
Toledo-Padrón, B., González Hernández, J. I., Rodríguez-López, C., et al. 2019, MNRAS, 488, 5145
Turnpenney, S., Nichols, J. D., Wynn, G. A., & Burleigh, M. R. 2018, ApJ, 854, 72
van der Walt, S., Colbert, S. C., & Varoquaux, G. 2011, CSE, 13, 22
VanderPlas, J. T. 2018, ApJS, 236, 16
Vedantham, H. K., Callingham, J. R., Shimwell, T. W., et al. 2020, NatAs, 4, 577

Virtanen, P., Gommers, R., Oliphant, T. E., et al. 2020, Nat. Methods, 17, 261
Wallace, L., Hinkle, K., & Livingston, W. C. 1993, An atlas of the photospheric spectrum from 8900 to 13600 cm^{-1} (7350 to 11230 [angstroms]), NSO Technical Report, 93-001, National SOlar Observatory
Wallace, L., & Livingston, W. C. 1992, An atlas of a dark sunspot umbral spectrum from 1970 to 8640 cm^{-1} (1.16 to 5.1 [microns]), NSO Technical Report, 92-001, National Solar Observatory
Wallace, L., Livingston, W. C., Bernath, P. F., & Ram, R. S. 1999, An atlas of the sunspot umbral spectrum in the red and infrared from 8900 to 15,050 cm^{-1} (6642 to 11,230 [angstroms]), revised, NSO Technical Report, 99-001, National Solar Observatory
Wise, A. W., Dodson-Robinson, S. E., Bevenour, K., & Provini, A. 2018, AJ, 156, 180
Zarka, P. 2007, P&SS, 55, 598
Zechmeister, M., Dreizler, S., Ribas, I., et al. 2019, A&A, 627, A49
Zechmeister, M., & Kürster, M. 2009, A&A, 496, 577
Zechmeister, M., Reiners, A., Amado, P. J., et al. 2018, A&A, 609, A12